CeO$_2$ for Water Remediation: Comparison of Various Advanced Oxidation Processes

Roberto Fiorenza [1], **Stefano Andrea Balsamo** [1], **Luisa D'Urso** [1], **Salvatore Sciré** [1], **Maria Violetta Brundo** [2], **Roberta Pecoraro** [2], **Elena Maria Scalisi** [2], **Vittorio Privitera** [3] **and Giuliana Impellizzeri** [3],*

[1] Department of Chemical Sciences, University of Catania, Viale A. Doria 6, 95125 Catania, Italy; rfiorenza@unict.it (R.F.); stefano.balsamo@phd.unict.it (S.A.B.); ldurso@unict.it (L.D.); sscire@unict.it (S.S.)

[2] Department of Biological, Geological and Environmental Science, University of Catania, Via Androne 81, 95124 Catania, Italy; mvbrundo@unict.it (M.V.B.); roberta.pecoraro@unict.it (R.P.); scalisimariaelena90@gmail.com (E.M.S.)

[3] CNR-IMM, Via S. Sofia 64, 95123 Catania, Italy; vittorio.privitera@cnr.it

* Correspondence: giuliana.impellizzeri@ct.infn.it; Tel.: + 39 095 3785345

check for updates

Abstract: Three different Advanced Oxidation Processes (AOPs) have been investigated for the degradation of the imidacloprid pesticide in water: photocatalysis, Fenton and photo-Fenton reactions. For these tests, we have compared the performance of two types of CeO$_2$, employed as a non-conventional photocatalyst/Fenton-like material. The first one has been prepared by chemical precipitation with KOH, while the second one has been obtained by exposing the as-synthetized CeO$_2$ to solar irradiation in H$_2$ stream. This latter treatment led to obtain a more defective CeO$_2$ (coded as "grey CeO$_2$") with the formation of Ce^{3+} sites on the surface of CeO$_2$, as determined by Raman and X-ray Photoelectron Spectroscopy (XPS) characterizations. This peculiar feature has been demonstrated as beneficial for the solar photo–Fenton reaction, with the best performance exhibited by the grey CeO$_2$. On the contrary, the bare CeO$_2$ showed a photocatalytic activity higher with respect to the grey CeO$_2$, due to the higher exposed surface area and the lower band-gap. The easy synthetic procedures of CeO$_2$ reported here, allows to tune and modify the physico-chemical properties of CeO$_2$, allowing a choice of different CeO$_2$ samples on the basis of the specific AOPs for water remediation. Furthermore, neither of the samples have shown any critical toxicity.

Keywords: ceria; pesticide; photocatalysis; photo-Fenton; AOPs

1. Introduction

Among the environmental questions of the present, water pollution by emergent contaminants, such as pharmaceuticals and pesticides, is a serious problem, making their removal a challenging task [1]. In particular, the use of pesticides has increased over the years to improve the production of agricultural goods and to satisfy the contextual growth of world population. Pesticides are a wide group of chemical compounds classified as persistent hazardous pollutants owing to a very high time of retention in water and giving rise to accumulation in sediment and in water effluents. They are also easily transferred over a long distance [2]. Their presence in the environment, especially in water, even at low concentrations, is a serious problem for both living organisms and human health.

Advanced Oxidation Processes (AOPs) are among the new, green and performing solutions for the removal of pesticides from water [3,4]. In these processes, the oxidation of the hazardous contaminants is obtained through the production of highly reactive radical species, such as $^\bullet O_2^-$, $^\bullet O_3^-$, or OH$^\bullet$. Different AOPs can be simultaneously utilized to avoid the generation of by-products
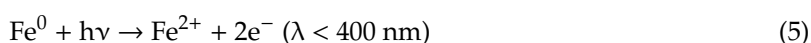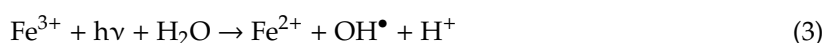
in treated water [5]. In this context, the photocatalysis and the Fenton process are two of the most promising AOPs [6]. The degradation of pesticides in water by means of photocatalysis allows to efficiently remove these pollutants with a moderate formation of secondary products and the selectivity of the process can be enhanced if peculiar materials (such as molecularly imprinted photocatalysts) are employed [7–10]. The hydroxyl radicals are formed in this process after the irradiation of a semiconductor photocatalyst with UV or a solar/visible light source with the consequent formation of photoelectrons in the conduction band and photoholes in the valence band of the photocatalyst [11]. The Fenton process involves the reaction between Fe^{2+} and hydrogen peroxide to give the hydroxyl radicals (reaction 1):

$$Fe^{2+} + H_2O_2 \rightarrow Fe^{3+} + OH^\bullet + OH^- \tag{1}$$

The further reaction of the ferric ions with the excess of H_2O_2 re-generates the ferrous ions with the formation of the hydroperoxyl radicals ($HOO^\bullet$) (reaction 2):

$$Fe^{3+} + H_2O_2 \rightarrow Fe^{2+} + HOO^\bullet + H^+ \tag{2}$$
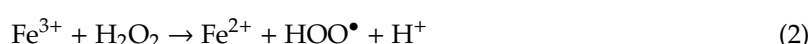
The regeneration of ferrous ions can be accelerated, enhancing also the efficiency of the overall degradation process, in the presence of visible or near ultraviolet irradiation (i.e., the photo-Fenton process, reactions 3-5), with the consequent formation of further hydroxyl radicals [12,13]. Furthermore, some Fe(III)–carboxylate complexes originated from the coordination of Fe^{3+}, and organic intermediates can adsorb in the UV–vis region, and other Fe^{2+} species can be formed through the ligand-to-metal charge transfer (LMCT) (reaction 4). Finally, also the zero-valent iron species can be considered a source of Fe^{2+} (reaction 5) [14].

$$Fe^{3+} + h\nu + H_2O \rightarrow Fe^{2+} + OH^\bullet + H^+ \tag{3}$$

$$[Fe^{3+} (RCO_2)]^{2+} + h\nu \rightarrow Fe^{2+} + CO_2 + R^\bullet \tag{4}$$

$$Fe^0 + h\nu \rightarrow Fe^{2+} + 2e^- \ (\lambda < 400 \ nm) \tag{5}$$

The photo-Fenton process was successfully applied in the degradation of various pesticides and pharmaceuticals under solar light irradiation [15,16].

Among the various semiconductors used for the photocatalytic applications, recently, cerium oxide (CeO_2, commonly called *ceria*), a largely used catalyst in many thermo-catalytic reactions [17,18], was examined as an alternative to the most used metal oxide photocatalysts (such as TiO_2 and ZnO [19–22]). The most attractive properties of CeO_2 are: the lower band-gap (around 2.7–2.8 eV) compared to TiO_2 and ZnO, making the material sensitive to visible light; the presence of empty 4f energy levels that facilitate the electron transfers; the high stability in the reaction medium; the high oxygen mobility related to the reversible Ce^{4+}/Ce^{3+} transformation, and the ability to form nonstoichiometric oxygen-deficient CeO_{2-x} oxide [23]. The presence of defect centres in the CeO_2, together with the high oxygen mobility and the consequential redox properties can be exploited in the Fenton-like reactions, that in this case, are different to the radical-attacking mechanism of conventional iron-based Fenton process, are driven by the interaction between the hydrogen peroxide and the surface defective Ce^{3+} centres (reactions 6–8, [24,25]):

$$Ce^{3+} + H_2O_2 \rightarrow Ce^{4+} + OH^\bullet + OH^- \tag{6}$$

$$H_2O_2 + OH^\bullet \rightarrow H_2O + HOO^\bullet \tag{7}$$

$$Ce^{4+-} + HOO^\bullet \rightarrow Ce^{3+} + H^+ + O_2 \tag{8}$$

The conventional iron species catalysts in the Fenton process require a strict operating pH range (between 3 and 4), thus increasing the overall process cost, whereas with CeO_2 it is possible to work at neutral pH [26].

On the basis of the above considerations, in this work we have studied the degradation of a largely used insecticide, i.e., the imidacloprid ($C_9H_{10}ClN_5O_2$), by the comparison between three different AOPs: solar photocatalysis, Fenton and solar photo-Fenton, taking advantage of the wide versatility of CeO_2 that can be used both as a photocatalyst and as a Fenton-like reagent.

The imidacloprid (hereafter called "IMI") is a neonicotinoid pesticide, which acts similarly to the natural insecticide nicotine [27]. Although IMI is not directly used in water, it is commonly transferred to water channels, and it presents a high leachability [28,29]. For its high toxicity, solubility, and stability, the presence of IMI in water even at low concentrations is a serious environmental concern.

The Fenton-like process through ceria is activated by the presence of non-stoichiometric Ce^{3+} centres on the surface of CeO_2 (reaction 6, [30,31]). One of the simpler methods to induce these defects is the exposure of CeO_2 to sunlight [32]. Indeed, the interaction of CeO_2 with the efficient UV solar photons (i.e., the photons with an energy higher than the band-gap of CeO_2) led to a release of the labile ceria surface oxygens with the formation of CeO_{2-x} defects. After the loss of oxygen, the cerium atoms adopted the most stable configuration, i.e., the Ce^{3+} oxidation state.

In this context, we have synthetized two different types of CeO_2: the first through one of the most employed preparation procedures for this oxide, as the precipitation with KOH from a cerium nitrate solution [23,33]; the second type using the same synthesis but irradiating the samples just after calcination with a solar lamp and in the presence of a H_2 flow, with the aim to further increase the surface defects on CeO_2. Interestingly, with this original modified strategy we have obtained a "grey CeO_2" instead of the typical yellow coloured ceria. The possibility to generate further defects on CeO_2 with solar exposure in a reducing atmosphere was especially exploited, due to a synergistic mechanism able to in situ provide the Ce^{3+} species, mainly in the solar photo-Fenton tests.

2. Results and Discussion

2.1. Characterizations of Bare CeO₂ and Grey (Modified) CeO₂

The first difference between the bare CeO_2 and the CeO_2 exposed to the solar irradiation (for 3 h) in H_2 flow at room temperature, is the change of the powder color. Figure 1 reports two photos of the synthetized materials: un-modified CeO_2 appears yellow in color, while modified CeO_2 is grey. This latter sample is coded as "grey CeO_2". Interestingly, we have noted that only the contemporaneous treatment with solar irradiation and H_2 flow could obtain the grey CeO_2, whereas each single treatment alone did not alter the structural and chemical properties of bare CeO_2.
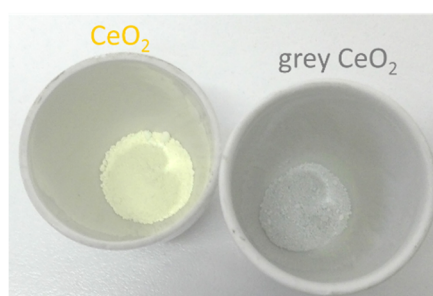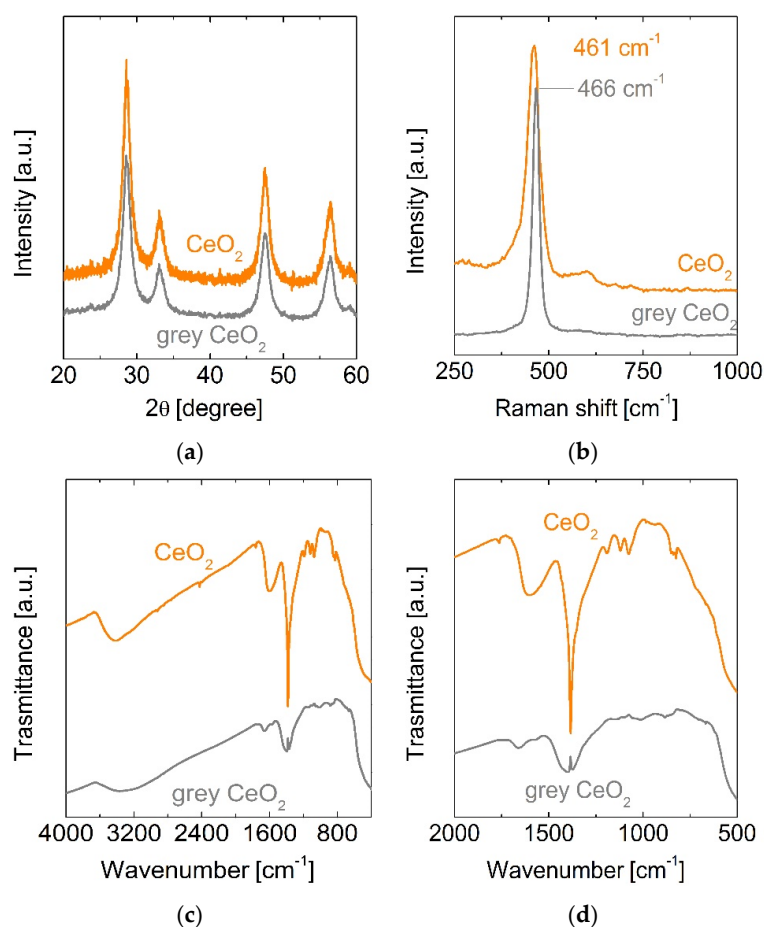

Figure 1. Photo of the as-synthetized powders.

The differences in the physico-chemical properties of bare CeO_2 and grey CeO_2 were illustrated in Figure 2, where the XRD patterns (Figure 2a), the Raman (Figure 2b), and the FTIR (Figure 2c,d) spectra are reported.

Figure 2. (**a**) XRD patterns, (**b**) Raman spectra, (**c**) FTIR spectra of the synthetized samples, and (**d**) FTIR zoom of the "carbonate" zone.

Both the samples exhibited the typical XRD pattern of ceria in the fluorite crystalline phase (Figure 2a), with the reflections at 2θ values of 28.6 (1 1 1), 33. 1 (2 0 0), 47.4 (2 2 0), and 56.4 (3 1 1) [34]. No substantial variation was detected in the grey CeO_2 compared to bare oxide, apart from a slight intensity decrease and a difference in the average crystallite size: 6.8 ± 0.8 nm for bare CeO_2 respect to 11.3 ± 1.1 nm for grey CeO_2, calculated using the Scherrer equation on the main diffraction peak of ceria 2θ = 28.6 (1 1 1). This size enhancement of grey CeO_2 was related to the occurrence of the formation of defects inside the crystalline structure of CeO_2 caused by the solar irradiation in the H_2 stream. Furthermore, in accordance with the literature data [26,35], the intensity diminution observed in the grey CeO_2 can be reasonable connected to a decrease in crystallinity due to the formation of CeO_{2-x} defects.

Interestingly, analyzing the Raman spectra of the samples (Figure 2b), the peak at 461 cm^{-1} of the CeO_2 was blue-shifted by 5 cm^{-1} in the grey CeO_2. The Raman peak at 461 cm^{-1} identifies the F_{2g} skeletal vibration of the cubic fluorite structure [36]. The position of this peak is influenced by the distortion of the Ce-O bonds [32]. Consequently, the treatment of grey CeO_2 led to a more defective structure with the modification of the cubic structure of CeO_2, resulting in the Raman shift. However, in the as-synthesized bare CeO_2, an imperfect crystalline stoichiometry was detected, being the small shoulder at about 600 cm^{-1} (more intense in the bare CeO_2), ascribed to Frenkel-type oxygen vacancies [37]. Other differences can be seen in the FTIR spectra (Figure 2c). The bands at about and 1620 cm^{-1} are attributed to the stretching and the bending of the O-H groups of residual water molecules respectively, whereas the group of bands in the range 1600–500 cm^{-1} are related to the presence of carbonates due to the interaction of the atmospheric carbon dioxide with ceria [38].

From the zoomed spectra illustrated in Figure 2d, it is possible to note the formation of different carbonate species. Specifically, for bare CeO_2, the high intense band at 1385 cm^{-1} is due to monodentate carbonates, whereas the bands at 1190 and 1120 cm^{-1} are related to the bridged carbonate species. Finally, the bands at 1071 and 839 cm^{-1} indicated the formation of hydrocarbonates [39–41]. In the grey CeO_2, the band assigned to the monodentate carbonate was broader and shifted at 1395 cm^{-1}, whereas the low intense bands at 1012 and 872 cm^{-1} can be also be assigned for this sample to the presence of hydrocarbonates, whereas there is no evidence of the formation of monodentate carbonates. It is clear that the surface interaction sites in the grey CeO_2 were changed compared to un-treated CeO_2. This can be reasonably related to the more defective surface of grey CeO_2.

The textural properties of the CeO_2 samples are displayed in the Figure 3. Both the materials displayed a N_2 adsorption–desorption isotherm of type III, with a H3 hysteresis loop (Figure 3a), indicating the presence of macro-meso slit-shaped pores [42]. The treatment with solar lamp in H_2 flow led to a decrease in the Brunauer–Emmett–Teller (BET) surface area. The grey CeO_2 exhibited a lower surface area (67 ± 1 m^2/g) than CeO_2 (81 ± 1 m^2/g). This decrease can be reasonably due to the agglomeration of CeO_2 particles caused by the irradiation treatment under solar lamp in H_2 flow, as further confirmed by the increase in mean crystalline size calculated by XRD. As a consequence, it was verified a shift towards large pores in the Barrett, Joyner and Halenda (BJH) pore size distribution curves (Figure 3b), with the mean pore size of the grey CeO_2 higher (58 ± 1 nm) with respect to bare CeO_2 (36 ± 1 nm). This size increase, verified by the grey CeO_2, is strictly correlated with the peculiar treatment of this latter sample, i.e., the simultaneous utilization of the simulated solar radiation and the H_2 stream. As stated before, according to the work of Aslam et al. [32], the solar light alone did not caused any change in the mean size of bare CeO_2; however, we used a more focused solar lamp than in ref. [32], which led to a slight heating of the sample (from room temperature to about 40 °C). On the contrary, the irradiation in a reductive atmosphere (H_2 stream) promoted the formation of numerous oxygen vacancies, a process characterized with an increase in the internal pressure inside the ceria crystalline structure with a consequent interatomic bond cleavage [43]. Reasonably, this process resulted in an agglomeration with a measurable size increase in the grey CeO_2 particle size. The same linear correlation between the increase in mean crystalline size, and the decrease in the BET surface area was already reported in the literature with other CeO_2-based samples [44,45]. The formation of defects did not alter the morphology of the CeO_2 materials, that, if prepared by chemical precipitation, are usually characterized by a random stacking of particles [23,32].

(a)

(b)
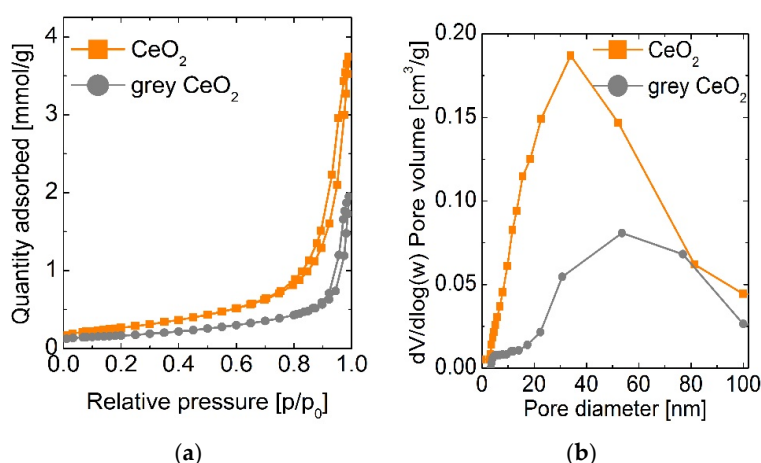
Figure 3. (**a**) N_2 adsorption–desorption isotherms of the CeO_2 samples; (**b**) pore size distribution curve of the analyzed samples evaluated by means of the Barrett, Joyner and Halenda (BJH) method.

The UV-vis Diffuse Reflectance spectra of the CeO_2 powders are displayed in Figure 4a where the reflectance function (Kubelka–Munk function) is plotted versus the wavelength. A slight variation in the absorption features was detected for grey CeO_2 with a shift at lower wavelengths that results in

a slightly higher optical band-gap (3.1 ± 0.3 eV) compared to bare CeO_2 (2.7 ± 0.3 eV) estimated by graphing the modified Kubelka–Munk function versus the eV (Figure 4b) [46]. The lower band-gap of CeO_2 (activation wavelength ≤ 460 nm) is suitable to exploit, together with the UV portion, a part of visible component of the solar light, whereas the grey CeO_2 with a higher band-gap (activation wavelength ≤ 400 nm) will be preferentially activated by the solar UV photons.
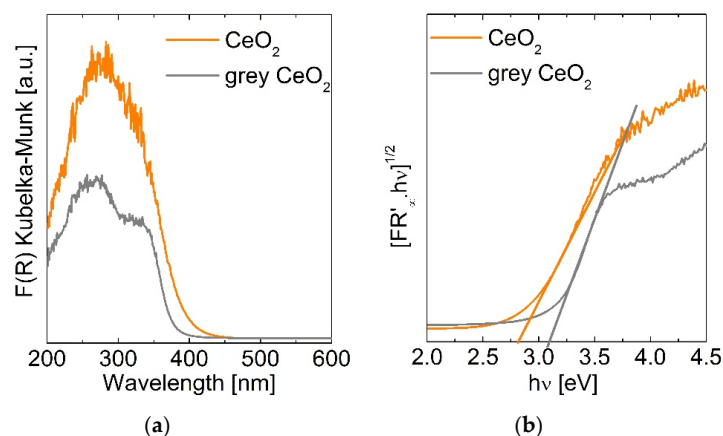
Figure 4. (**a**) UV-vis Diffuse Reflectance spectra of CeO_2 powders; (**b**) estimation of the optical band-gap of the samples by means of the modified Kubelka–Munk function.
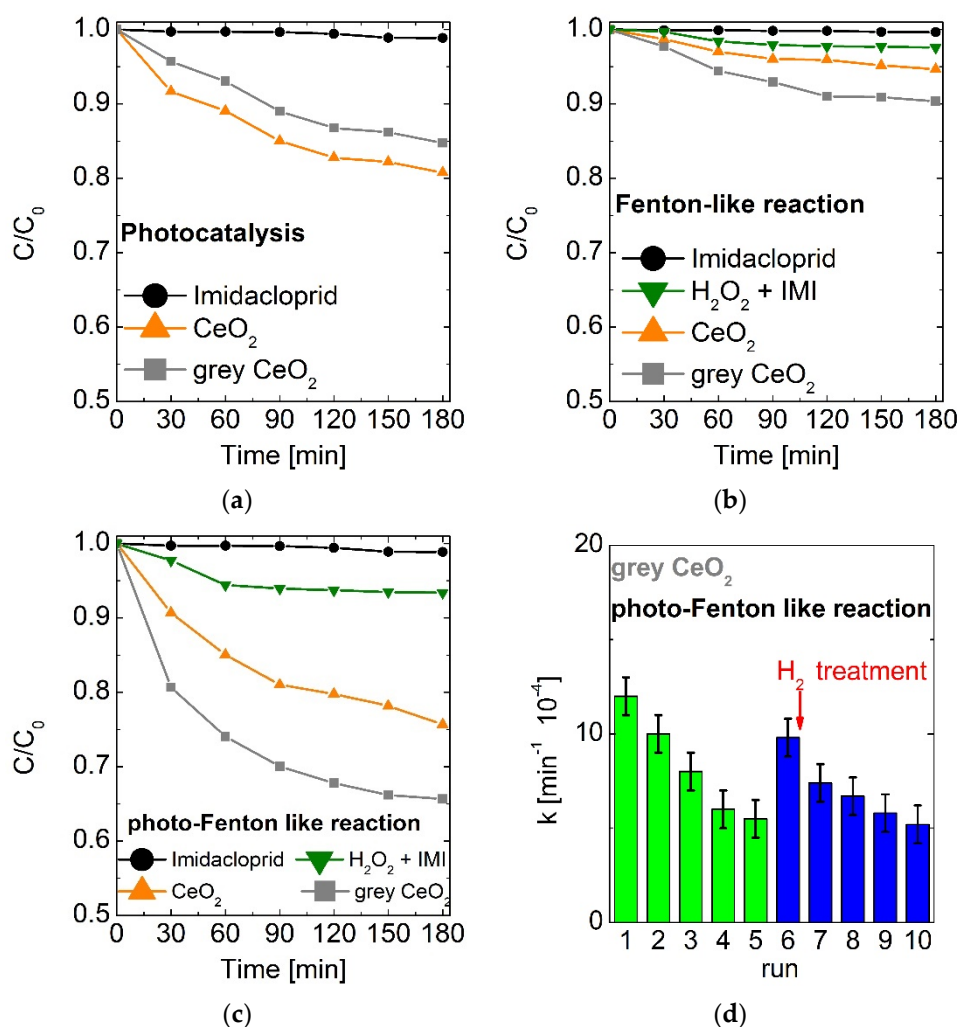
For the photocatalytic degradation of the IMI and especially for the Fenton and photo-Fenton reactions, it is fundamental that the presence of Ce^{3+} defects on the surface of CeO_2. To establish the presence of these defect states, the XPS analysis was performed and the results are illustrated in Figure 5. In accordance with the literature data, the Ce $3d_{5/2}$ state involves the v, v′, v″ and v‴ component, whereas the u, u′, u″ and u‴ components are related to the Ce $3d_{3/2}$ state [47–50]. The v′ and u′ components indicate the presence of Ce^{3+}, whereas the peak at 916.4 eV (u‴) for CeO_2 and at 916.8 eV for the grey CeO_2 are the typical fingerprint of Ce^{4+} [48–50]. It is clearly visible from Figure 5, as the component v′ at 885.2 eV of Ce^{3+} is intense for grey CeO_2 whereas the same signal is absent in the bare CeO_2. The u′ signal is covered to the u and u″ components in both the samples. Furthermore, it is possible to note that, as the ratio between the v‴ and u components is different and shifted of about 0.5 eV, as for the v component, compared to un-modified CeO_2. This is another indication of the modification of the ceria surface sites with the higher presence of Ce^{3+} states in the grey CeO_2 [50]. The irradiation with solar lamp in H_2 stream thus induced the formation of CeO_{2-x} defects on the surface of CeO_2, as also confirmed by the Raman spectroscopy, with a consequent modification to the surface chemical composition of ceria, as also indirectly corroborated by the FTIR with the formation of different carbonate species in the two CeO_2 samples.
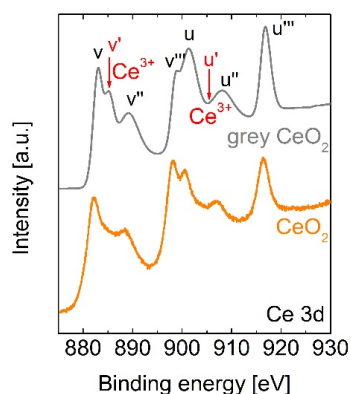
Figure 5. XPS spectra of the CeO_2 samples.

2.2. (Photo)catalytic Activity

We have compared the (photo)catalytic activity of the synthetized sample in the degradation of the IMI pesticide. Three different AOPs were investigated: a) the photocatalytic oxidation (Figure 6a) utilized as an irradiation source a solar lamp; b) the Fenton reaction (Figure 6b), adding 5 mL of H_2O_2 (3%, 0.9M) in the reaction mixture, c) the photo-Fenton reaction (Figure 6c) utilizing both the solar lamp and the hydrogen peroxide.

Figure 6. (**a**) Photocatalytic degradation of imidacloprid (IMI) under solar light irradiation, (**b**) Fenton-like reaction, (**c**) photo-Fenton like reaction on the CeO_2-based samples, (**d**) photo-Fenton like reaction utilizing grey CeO_2 in different runs.

The solar photodegradation of pesticides required harder conditions in comparison to the degradation of other pollutants (for example, dyes) [51,52]. As a result, even utilizing TiO_2 (the most investigated photocatalyst), the degradation efficiency is not so high [7,53]. Furthermore, in accordance with our preceding work [7], and the literature data [54,55], as confirmed for all the AOPs investigated, the IMI degradation is characterized by the formation of various by-products as amine and chloro-pyridine species. The reaction mechanism involves the breaking of C–N and the N–N bonds followed by the formation of small molecules, such as chlorine dioxide, nitrogen oxides species, water and carbon dioxide [7,54,55]. The reported degradation percentage of IMI (i.e., the variation of the IMI concentration respect to the initial IMI concentration) was low even through photocatalysis [54–56], solar photo-Fenton [57], or UV-A photolysis [28]. In particular, with UV irradiation it is possible to obtain a complete photolysis of IMI after

a long time of irradiation (about 10 h) [28], whereas in our precedent work [7] with molecularly imprinted TiO_2 samples, it was possible to selectively photodegrade IMI even in a pesticide mixture, although the degradation efficiency did not exceed 40% with a partial mineralization of ~35% (evaluated by the Total Organic Carbon, TOC, analysis) after 3 h of UV irradiation. Kitsiou et al. [57] found that the reaction efficiency can be improved utilizing a combination of photo-Fenton under UV-A irradiation and TiO_2, due to the synergism between the homogenous iron catalyst and the heterogeneous TiO_2 photocatalyst (~80% of degradation after 2 h of UV-A irradiation and ~60% of TOC mineralization), whereas only the solar homogenous photo-Fenton with iron reached ~50% for both degradation and removal of organic carbon after 3 h of UV-A irradiation. The most promising result was obtained by Sharma et al. [54] with a particular TiO_2 supported on mesoporous silica SBA-15, that allowed to achieve ~90% IMI degradation after 3 h of solar irradiation. In this contest, the obtained (photo)catalytic performances of CeO_2 for the degradation of IMI described in this work are in line with the results obtained with the TiO_2-based materials.

Figure 6a reports the photocatalytic degradation of the synthetized powders. In the test without catalysts, (black line in Figure 6a) no substantial variations in the initial concentration of IMI was measured, as expected. On the other hand, after 3 h of solar light irradiation the bare CeO_2 was able to degrade around the 20% of the initial concentration of IMI, whereas the grey CeO_2 showed a slightly lower performance (~16%). This can be reasonably explained considering the lower surface area and/or the slightly higher band-gap of grey CeO_2 with respect to the un-modified CeO_2.

The catalytic activity through the Fenton reaction (Figure 6b) is significantly lower compared to the photocatalytic tests (the test was carried out without irradiation). In these tests, no substantial degradation of IMI was measured in the run carried out without catalysts, but with H_2O_2 (Figure 6b, olive line).

As explained in the Introduction (see reactions 6-8), the Fenton process requires the presence and the fast regeneration of Ce^{3+} defect sites. For this reason, differently to the photocatalytic tests, the grey CeO_2 is more active than the bare CeO_2. As detected by Raman and XPS measurements, the un-modified CeO_2 exhibited a much lower presence of defect centres with respect to grey CeO_2. Conversely, despite the major presence of surface defects in the grey CeO_2, the degradation percentage measured on grey CeO_2 after 3 h of reaction in the Fenton-like test (~10%) was lower compared to the degradation efficiency of the photocatalytic test (~16%) obtained with the same sample, which pointed to the slow regeneration of the Ce^{3+} sites.

As reported, the Fenton-like reaction with CeO_2 involves the formation of peroxide species on the surface of ceria due to the complexation of H_2O_2 with Ce^{3+} sites [25,30,58]. These peroxide species are chemically stable and can saturate the surface of CeO_2, hindering the adsorption and subsequent oxidation of the organic target contaminant [25,30,58]. Indeed, a higher concentration of H_2O_2 (superior to 3%, i.e., 0,9 M) both in the Fenton and in the photo-Fenton like reactions led to a considerable decrease in the catalytic activity of the grey CeO_2 (the highest performing sample for these tests, Figure S1). The regeneration and the further formation of Ce^{3+} defect centres are, in this way, crucial steps.

Interestingly, in the photo-Fenton like reaction (Figure 6c), the grey CeO_2 displayed the best performance (~35% of degradation), comparing all the investigated AOPs with the two CeO_2 samples. The solar irradiation could boost the further formation of Ce^{3+} sites. An indirect confirmation is derived from the slight enhancement of the catalytic activity of bare CeO_2 (25%) compared to the solar photocatalytic test (20%) that can be attributed to the formation of in situ oxygen vacancies in the surface of bare CeO_2 which can react with the hydrogen peroxide.

As reported in the literature [25,32], the irradiation of ceria with photons which possess energy higher than the CeO_2 band-gap can exploit the following reaction:

$$CeO_2 + h\nu \ (E \geq E_g) \rightarrow Ce^{+3,+4}O_{2-x} + x/2 \ O_2 \tag{9}$$
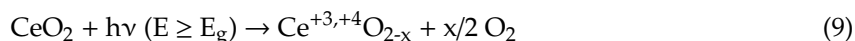
The interaction of the highly energetic photons with the surface of CeO_2 leads to the loss of surface oxygen, thus allowing the formation of the Ce^{3+} states. The same reaction was exploited during the

preparation of grey CeO_2, where the formation of Ce^{3+} was further increased due to the reducing atmosphere. Therefore, with the grey CeO_2, owing to a higher number of defective centres compared to bare ceria (as shown by XPS and Raman analyses), it is possible to reach the best performance in the degradation of IMI by the photo-Fenton-like reaction. Furthermore, the contemporaneous presence of the hydrogen peroxide and the solar irradiation enhances the formation of hydroxyl radicals through the photolytic decomposition of H_2O_2, as confirmed by the experiment carried out without a catalyst (H_2O_2 + IMI) that led to a slight variation in the initial concentration of IMI (Figure 6c, olive line).

It is important to highlight that, in the photocatalytic tests, the occurrence of the photon interaction (reaction 9, reported above) can be exploited, but it has a minor role in determining the final performance. The presence of Ce^{3+} was usually connected in the literature [59–61] to an improvement in the photocatalytic performance, especially under visible light irradiation, due to the presence of as-formed oxygen vacancies that shift the absorption of CeO_2 towards the visible-light region, improving the separation of the photogenerated charge carriers. However, the mean crystalline size and consequently the active surface area of the photocatalyst contribute considerably to the overall photocatalytic activity [34,62], as in our case, where the influence of the surface area is more preponderant than the effect of defects. For this reason, in the solar photocatalytic test, the bare CeO_2 (BET surface area of 81 m^2/g) was more active than grey CeO_2 (BET surface area of 67 m^2/g).

Finally, to test the reusability of grey CeO_2, different photo-Fenton like reaction runs were performed on the same sample. In Figure 6d, the variation in the kinetic constant (referring to a first order kinetic [7] is reported with respect to the various runs. After five runs, the kinetic constant decreases from $12 \pm 1 \cdot 10^{-4}$ min^{-1} to $5.5 \pm 0.6 \cdot 10^{-4}$ min^{-1}, highlighting that the continuous redox $Ce^{3+} \rightarrow Ce^{4+}$ process on the surface of grey ceria led to a progressive deactivation of the catalyst, reasonably for the saturation of the surface sites with the products of IMI degradation. Nevertheless, when the same sample were pre-treated before the tests in the H_2 flow at room temperature for 1 h, it was possible to exploit an almost total reversibility of grey CeO_2 in the photo-Fenton-like reaction. In fact, the kinetic constant raised to $10 \pm 1 \cdot 10^{-4}$ min^{-1} in run 6 and went back to $5.0 \pm 0.5 \cdot 10^{-4}$ min^{-1} after the subsequent other four runs, pointing to the crucial role of H_2 in the restoring the Ce^{3+} sites on grey CeO_2.

The comparison with the commercial TiO_2 P25 Degussa (Figure 7) showed, as in the photocatalytic test, that bare CeO_2 had a comparable catalytic behaviour with respect to TiO_2 (Figure 7a), whereas this latter sample exhibited no substantial activity in the Fenton-like test (Figure 7b), and a lower activity compared to CeO_2 and grey CeO_2 in the photo-Fenton test (Figure 7c). This pointed out that, both for Fenton and photo-Fenton like reactions, the CeO_2-based materials are better-performing than the commercial TiO_2. As reported [63,64], the bare TiO_2 without structural (i.e., incorporation of surface defects) or chemical (as the formation of composites with iron oxides) modifications is not able to promote Fenton-like reactions.
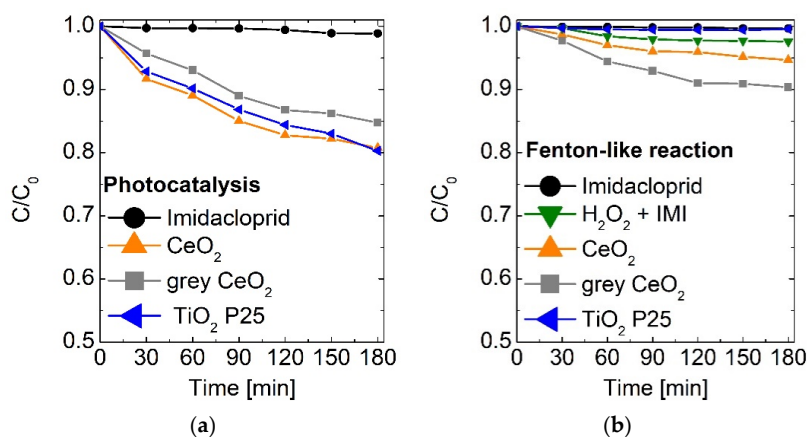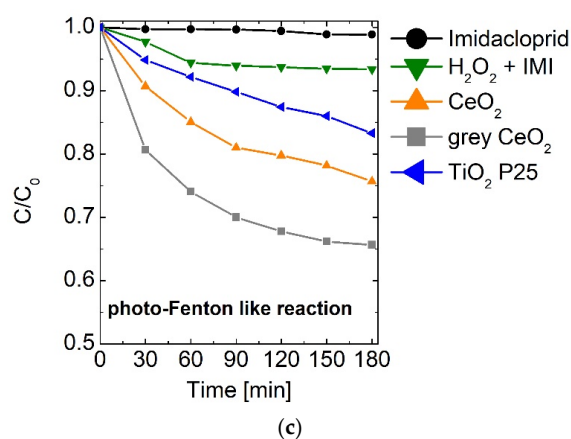

Figure 7. *Cont.*

(**c**)

Figure 7. (**a**) Photocatalytic degradation of IMI under solar light irradiation, (**b**) Fenton-like reaction, (**c**) photo-Fenton like reaction on the analyzed samples.

These data demonstrate the possibility of modifying and tuning the physico-chemical properties of CeO_2 with simple treatments, such as the solar light irradiation in a H_2 stream, so to maximize the catalytic performance. It is important to highlight, finally, that the CeO_2 sample simply treated with H_2 or irradiated with a solar lamp without an H_2 stream did not show substantial changes compared to bare CeO_2 in the degradation performance of IMI in all the AOPs investigated.

2.3. Tocixity Tests

*Artemia salina* dehydrated cysts were employed for the acute toxicity test.

Artemia salina nauplii can readily ingest fine particles smaller than 50 μm [65], and it is a non-selective filter-feeder organism. For these reasons, it is currently considered as a good model organism to assess in vivo nanoparticles toxicity, as previously demonstrated [66].

Low mortality percentages were evidenced after 24 and 48 h of exposure (Table 1), at different concentrations of both powders (bare CeO_2 and grey CeO_2). Statistical analysis, carried out by one-way ANOVA test, gave no significant values for all the immobilization percentages nor treated groups after 24 and 48 h of exposure nor between treated and control (Ctrl, i.e., without metal oxide particles) groups ($p > 0.05$). The percentages of immobilized nauplii are reported in the Table 1. These data pointed to the low critical toxicity of the examined powders. Furthermore, it is possible to note that the modification of CeO_2 led to have a lower mortality with respect to the bare CeO_2.

Table 1. Percentages of immobilized nauplii after exposition to CeO_2 (bare CeO_2 and grey CeO_2) at three different concentrations for 24 and 48 h.

Sample	Ctrl	10^{-1}	10^{-2}	10^{-3}
Bare CeO_2	1.6% (24 h) 6.6% (48 h)	11.6% (24 h) 28.3% (48 h)	6.6% (24 h) 23.3% (48 h)	3.3% (24 h) 21.6% (48 h)
Grey CeO_2	3.3% (24 h) 8.3% (48 h)	8.3 % (24 h) 23.3% (48 h)	6.6% (24 h) 18.3% (48 h)	4.0% (24 h) 15.0% (48 h)

Figure 8 shows *Artemia salina* nauplii treated with bare CeO_2 for 24 h, 48 h and untreated nauplii (i.e., the controls).
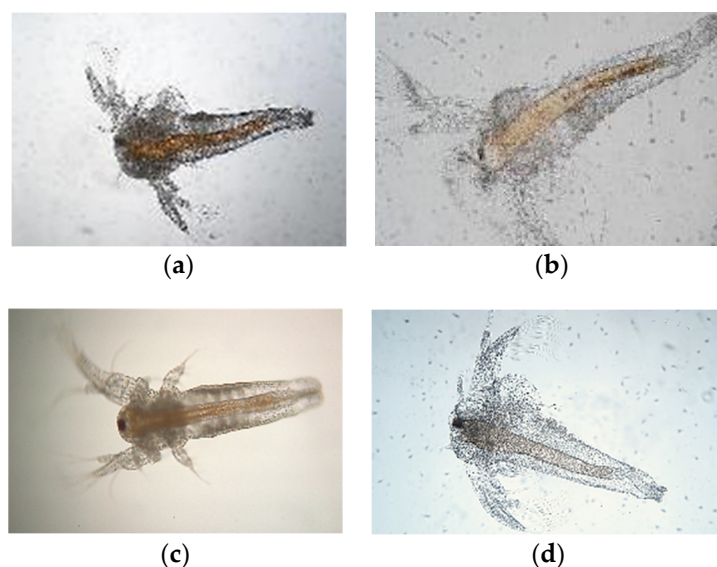
Figure 8. *Artemia salina* nauplii: nauplii exposed to bare CeO_2 for 24 h (**a**), nauplii exposed to bare CeO_2 for 48 h (**b**), control at 24 h (**c**), control at 48 h (**d**).

3. Materials and Methods

3.1. Samples Preparation

The bare CeO_2 was prepared via chemical precipitation from $Ce(NO_3)_3 \cdot 6H_2O$ (Fluka, Buchs, Switzerland) at pH > 8 utilizing a solution of KOH (1M, Fluka, Buchs, Switzerland). The obtained slurry was maintained under stirring at 80 °C for 3 h. After digestion for 24 h, it was filtered, washed with deionized water several times, and dried at 100 °C for 12 h. Finally, the powders were calcined in air at 450 °C for 3 h. The modified CeO_2 (grey CeO_2) was obtained with the same synthetic procedure reported above, but exposing the powders after calcination to the light of a solar lamp for 3 h (OSRAM Vitalux 300 W, 300–2000 nm; OSRAM Opto Semiconductors GmbH, Leibniz, Regensburg Germany) in a hydrogen stream (20 cc/min) at room temperature.

3.2. Samples Characterization

X-ray powder diffraction (XRD) measures were performed with a PANalytical X'pertPro X-ray diffractometer (Malvern PANalytical, Enigma Business Park, Grovewood Road, Malvern United Kingdom), employing a Cu Kα radiation. The identification of the crystalline phases was made comparing the diffractions with those of standard materials reported in the JCPDS Data File. Raman spectra were carried out with a WITec alpha 300 confocal Raman system (WITec Wissenschaftliche Instrumente und Technologie GmbH Ulm, Germany) with an excitation source at 532 nm under the same experimental condition reported in the ref. [67]. Fourier Transform Infrared Spectroscopy (FTIR) spectra were obtained in the range 4000–400 cm^{-1} using a Perkin Elmer FT-IR System 2000 (Perkin-Elmer, Waltham, MA, USA). The background spectrum was carried out with KBr. The textural properties of the samples were measured by N_2 adsorption–desorption at −196 °C with a Micromeritics Tristar II Plus 3020 (Micromeritics Instrument Corp. Norcross, USA), out-gassing the analysed materials at 100 °C overnight. UV-Vis-Diffuse Reflectance (UV-Vis DRS) spectra were obtained in the range of 200–800 nm using a Cary 60 spectrometer (Agilent Stevens Creek Blvd. Santa Clara, United States). X-ray photoelectron spectroscopy (XPS) measurements were recorded using a K-Alpha X-ray photoelectron spectrometer (Thermo Fisher Scientific Waltham, MA USA), utilizing the C 1 peak at 284.9 eV (ascribed to adventitious carbon) as a reference.

3.3. (Photo)catalytic Experiments

The photocatalytic tests were performed utilizing a solar lamp (OSRAM Vitalux 300 W, 300–2000 nm, OSRAM Opto Semiconductors GmbH, Leibniz, Regensburg Germany) irradiating a jacketed Pyrex batch reactor, kept at 25 °C. A total of 50 mg of powder was suspended in 50 mL of the reactant solution containing 5×10^{-5} M of IMI (Sigma-Aldrich, Buchs, Switzerland). The reaction mixture was stirred for 120 min in the dark so as to achieve the adsorption/desorption equilibrium. During the tests, aliquots of the suspension were withdrawn at a given time interval to measure the IMI concentration by means of Cary 60 UV–vis spectrophotometer (Agilent Stevens Creek Blvd. Santa Clara, United States). The IMI degradation was evaluated by following the absorbance peaks at 270 nm in the Lambert–Beer regime, reporting the C/C_0 ratio as a function of time t, where C is the concentration of the contaminant at the time t, while C_0 is the starting concentration of the pollutant. The Fenton-like reaction was carried out with the same apparatus described above, adding 5 mL of hydrogen peroxide (3%, 0.9 M Fluka, Buchs, Switzerland) in the reactor without irradiation; in the photo-Fenton-like tests the solar light irradiation was employed, too. In all the catalytic tests the experimental error was 1%, i.e., within the symbol size.

3.4. Toxicity Tests

Artemia salina dehydrated cysts were used for the acute toxicity test. Cysts (Hobby, Germany) were hydrated in ASPM seawater solution (ASPM is an artificial seawater made of: NaCl = 26.4 g, KCl = 0.84 g, $CaCl_2 \cdot H_2O$ = 1.67 g, $MgCl \cdot H_2O$ = 4.6 g, $MgSO_4 \cdot 7H_2O$ = 5.58 g, $NaHCO_3$ = 0.17 g, and H_3BO_3 = 0.03 g) maintaining standard laboratory conditions (1.500 lux daylight; 26 ± 1 °C; continuous aeration), then nauplii hatched within 24 h.

Two stock solutions of CeO_2 (bare CeO_2 and grey CeO_2) were prepared after dilution in ASPM solution. Then, fresh suspensions with different concentrations of powders (10^{-1}, 10^{-2}, 10^{-3} mg/mL) were made starting from the stock suspensions (1 mg/10 mL). These solutions were vortexed for 30 s. One nauplius per well in 96-well microplates, was added with 200 μL of each different concentration of powder solutions. They were incubated at 26 °C for 24/48 h. The number of surviving nauplii in each well was counted under a stereomicroscope after 24/48 h. A control group was also set up with ASPM seawater solution only. Larvae were not fed during the bioassays.

At the end of the test, the endpoints (immobility, i.e., death) were evaluated with a stereomicroscope (Leica EZ4, Leica Microsystems Srl, Buccinasco (MI), Italy): a nauplium was considered to be immobile or dead if it could not move its antennae after slight agitation of the water for 10 seconds. Larvae that were completely motionless were counted as dead, and the percentages of mortality compared to the control were calculated. The death % of the crustacean for each concentration was calculated as follows: (n. dead nauplii/n. total animal treated 100). Data were analyzed for differences between the control and treatments using one-way ANOVA followed by Tukey's test, where $p < 0.05$ is considered significant and $p < 0.01$ extremely significant.

4. Conclusions

Different AOPs (photocatalysis, Fenton and photo-Fenton reactions) were investigated for the degradation of the IMI insecticide. Two CeO_2 samples were tested, one prepared with the conventional precipitation route and another one modifying the as-prepared CeO_2 by exposing it to solar light irradiation in a hydrogen stream. The latter treatment allowed to obtain a more defective ceria with increased performance in the solar photo-Fenton reaction. This hybrid AOP obtained the best degradation rate of the IMI. The photon interaction with the surface of CeO_2 led to a loss of oxygen with the formation of Ce^{3+} centers, which is essential to boost the degradation rate of the pesticide degradation through the photo-Fenton process. The solar irradiation in a reducing atmosphere could obtain a defective ceria that can be exploited to explore new synergisms between different AOPs for wastewater purification over non-conventional photocatalysts/Fenton materials. Furthermore, the investigated materials did not exhibit critical toxicity.

References

1. Salimi, M.; Esrafili, A.; Gholami, M.; Jonidi Jafari, A.; Rezaei Kalantary, R.; Farzadkia, M.; Kermani, M.; Sobhi, H.R. Contaminants of emerging concern: A review of new approach in AOP technologies. *Environ. Monit. Assess.* **2017**, *189*, 414. [CrossRef] [PubMed]

2. Katsikantami, I.; Colosio, C.; Alegakis, A.; Tzatzarakis, M.N.; Vakonaki, E.; Rizos, A.K.; Sarigiannis, D.A.; Tsatsakis, A.M. Estimation of daily intake and risk assessment of organophosphorus pesticides based on biomonitoring data—The internal exposure approach. *Food Chem. Toxicol.* **2019**, *123*, 57–71. [CrossRef] [PubMed]

3. Malakootian, M.; Shahesmaeili, A.; Faraji, M.; Amiri, H.; Silva Martinez, S. Advanced oxidation processes for the removal of organophosphorus pesticides in aqueous matrices: A systematic review and meta-analysis. *Process Saf. Environ. Prot.* **2020**, *134*, 292–307. [CrossRef]

4. Mazivila, S.J.; Ricardo, I.A.; Leitão, J.M.M.; Esteves da Silva, J.C.G. A review on advanced oxidation processes: From classical to new perspectives coupled to two- and multi-way calibration strategies to monitor degradation of contaminants in environmental samples. *Trends Environ. Anal. Chem.* **2019**, *24*, e00072. [CrossRef]

5. Dewil, R.; Mantzavinos, D.; Poulios, I.; Rodrigo, M.A. New perspectives for Advanced Oxidation Processes. *J. Environ. Manag.* **2017**, *195*, 93–99. [CrossRef] [PubMed]

6. Giménez, J.; Bayarri, B.; González, Ó.; Malato, S.; Peral, J.; Esplugas, S. Advanced Oxidation Processes at Laboratory Scale: Environmental and Economic Impacts. *ACS Sustain. Chem. Eng.* **2015**, *3*, 3188–3196. [CrossRef]

7. Fiorenza, R.; Di Mauro, A.; Cantarella, M.; Iaria, C.; Scalisi, E.M.; Brundo, M.V.; Gulino, A.; Spitaleri, L.; Nicotra, G.; Dattilo, S.; et al. Preferential removal of pesticides from water by molecular imprinting on TiO_2 photocatalysts. *Chem. Eng. J.* **2020**, *379*, 122309. [CrossRef]

8. Fiorenza, R.; Di Mauro, A.; Cantarella, M.; Privitera, V.; Impellizzeri, G. Selective photodegradation of 2,4-D pesticide from water by molecularly imprinted TiO_2. *J. Photochem. Photobiol. A Chem.* **2019**, *380*. [CrossRef]

9. Fiorenza, R.; Di Mauro, A.; Cantarella, M.; Gulino, A.; Spitaleri, L.; Privitera, V.; Impellizzeri, G. Molecularly imprinted N-doped TiO_2 photocatalysts for the selective degradation of o-phenylphenol fungicide from water. *Mater. Sci. Semicond. Process.* **2020**, *112*, 105019. [CrossRef]

10. Cantarella, M.; Di Mauro, A.; Gulino, A.; Spitaleri, L.; Nicotra, G.; Privitera, V.; Impellizzeri, G. Selective photodegradation of paracetamol by molecularly imprinted ZnO nanonuts. *Appl. Catal. B Environ.* **2018**, *238*, 509–517. [CrossRef]

11. Iervolino, G.; Zammit, I.; Vaiano, V.; Rizzo, L. Limitations and Prospects for Wastewater Treatment by UV and Visible-Light-Active Heterogeneous Photocatalysis: A Critical Review. *Top. Curr. Chem.* **2020**, *378*. [CrossRef] [PubMed]

12. Herney-Ramirez, J.; Vicente, M.A.; Madeira, L.M. Heterogeneous photo-Fenton oxidation with pillared clay-based catalysts for wastewater treatment: A review. *Appl. Catal. B Environ.* **2010**, *98*, 10–26. [CrossRef]

13. Babuponnusami, A.; Muthukumar, K. A review on Fenton and improvements to the Fenton process for wastewater treatment. *J. Environ. Chem. Eng.* **2014**, *2*, 557–572. [CrossRef]

14. Liu, X.; Zhou, Y.; Zhang, J.; Luo, L.; Yang, Y.; Huang, H.; Peng, H.; Tang, L.; Mu, Y. Insight into electro-Fenton and photo-Fenton for the degradation of antibiotics: Mechanism study and research gaps. *Chem. Eng. J.* **2018**, *347*, 379–397. [CrossRef]

15. Dutta, A.; Das, N.; Sarkar, D.; Chakrabarti, S. Development and characterization of a continuous solar-collector-reactor for wastewater treatment by photo-Fenton process. *Sol. Energy* **2019**, *177*, 364–373. [CrossRef]

16. De la Obra, I.; Ponce-Robles, L.; Miralles-Cuevas, S.; Oller, I.; Malato, S.; Sánchez Pérez, J.A. Microcontaminant removal in secondary effluents by solar photo-Fenton at circumneutral pH in raceway pond reactors. *Catal. Today* **2017**, *287*, 10–14. [CrossRef]

17. Sciré, S.; Fiorenza, R.; Gulino, A.; Cristaldi, A.; Riccobene, P.M. Selective oxidation of CO in H_2-rich stream over ZSM5 zeolites supported Ru catalysts: An investigation on the role of the support and the Ru particle size. *Appl. Catal. A Gen.* **2016**, *520*, 82–91. [CrossRef]

18. Fiorenza, R.; Spitaleri, L.; Gulino, A.; Sciré, S. High-Performing Au-Ag Bimetallic Catalysts Supported on Macro-Mesoporous CeO_2 for Preferential Oxidation of CO in H_2-Rich Gases. *Catalysts* **2020**, *10*, 49. [CrossRef]

19. Fiorenza, R.; Condorelli, M.; D'Urso, L.; Compagnini, G.; Bellardita, M.; Palmisano, L.; Sciré, S. Catalytic and Photothermo-catalytic Applications of TiO_2-CoO_x Composites. *J. Photocatal.* **2020**, *1*. [CrossRef]

20. Scuderi, V.; Amiard, G.; Sanz, R.; Boninelli, S.; Impellizzeri, G.; Privitera, V. TiO_2 coated CuO nanowire array: Ultrathin p–n heterojunction to modulate cationic/anionic dye photo-degradation in water. *Appl. Surf. Sci.* **2017**, *416*, 885–890. [CrossRef]

21. Di Mauro, A.; Fragalà, M.E.; Privitera, V.; Impellizzeri, G. ZnO for application in photocatalysis: From thin films to nanostructures. *Mater. Sci. Semicond. Process.* **2017**, *69*, 44–51. [CrossRef]

22. Vela, N.; Calín, M.; Yáñez-Gascón, M.J.; el Aatik, A.; Garrido, I.; Pérez-Lucas, G.; Fenoll, J.; Navarro, S. Removal of Pesticides with Endocrine Disruptor Activity in Wastewater Effluent by Solar Heterogeneous Photocatalysis Using ZnO/Na2S2O8. *Water Air Soil Pollut.* **2019**, *230*, 134. [CrossRef]

23. Bellardita, M.; Fiorenza, R.; Palmisano, L.; Sciré, S. Photocatalytic and photo-thermo-catalytic applications of cerium oxide based material. In *Cerium Oxide (CeO_2): Synthesis, Properties and Applications*; a Volume in Metal Oxides Series; Elsevier: Amsterdam, The Netherlands, 2020; ISBN 978-0-12-815661-2. [CrossRef]

24. Heckert, E.G.; Seal, S.; Self, W.T. Fenton-like reaction catalyzed by the rare earth inner transition metal cerium. *Environ. Sci. Technol.* **2008**, *42*, 5014–5019. [CrossRef] [PubMed]

25. Issa Hamoud, H.; Azambre, B.; Finqueneisel, G. Reactivity of ceria–zirconia catalysts for the catalytic wet peroxidative oxidation of azo dyes: Reactivity and quantification of surface Ce(IV)-peroxo species. *J. Chem. Technol. Biotechnol.* **2016**, *91*, 2462–2473. [CrossRef]

26. Zhang, N.; Tsang, E.P.; Chen, J.; Fang, Z.; Zhao, D. Critical role of oxygen vacancies in heterogeneous Fenton oxidation over ceria-based catalysts. *J. Colloid Interface Sci.* **2020**, *558*, 163–172. [CrossRef] [PubMed]

27. Hayat, W.; Zhang, Y.; Hussain, I.; Huang, S.; Du, X. Comparison of radical and non-radical activated persulfate systems for the degradation of imidacloprid in water. *Ecotoxicol. Environ. Saf.* **2020**, *188*, 109891. [CrossRef] [PubMed]

28. Wamhoff, H.; Schneider, V. Photodegradation of imidacloprid. *J. Agric. Food Chem.* **1999**, *47*, 1730–1734. [CrossRef] [PubMed]

29. Tišler, T.; Jemec, A.; Mozetič, B.; Trebše, P. Hazard identification of imidacloprid to aquatic environment. *Chemosphere* **2009**, *76*, 907–914. [CrossRef]

30. Zang, C.; Yu, K.; Hu, S.; Chen, F. Adsorption-depended Fenton-like reaction kinetics in CeO_2-H_2O_2 system for salicylic acid degradation. *Colloids Surf. A Physicochem. Eng. Asp.* **2018**, *553*, 456–463. [CrossRef]

31. Xu, L.; Wang, J. Magnetic nanoscaled Fe_3O_4/CeO_2 composite as an efficient fenton-like heterogeneous catalyst for degradation of 4-chlorophenol. *Environ. Sci. Technol.* **2012**, *46*, 10145–10153. [CrossRef]

32. Aslam, M.; Qamar, M.T.; Soomro, M.T.; Ismail, I.M.I.; Salah, N.; Almeelbi, T.; Gondal, M.A.; Hameed, A. The effect of sunlight induced surface defects on the photocatalytic activity of nanosized CeO_2 for the degradation of phenol and its derivatives. *Appl. Catal. B Environ.* **2016**, *180*, 391–402. [CrossRef]

33. Fiorenza, R.; Spitaleri, L.; Gulino, A.; Scirè, S. Ru–Pd bimetallic catalysts supported on CeO_2-MnO_x oxides as efficient systems for H_2 purification through CO preferential Oxidation. *Catalysts* **2018**, *8*, 203. [CrossRef]

34. Fiorenza, R.; Bellardita, M.; Barakat, T.; Scirè, S.; Palmisano, L. Visible light photocatalytic activity of macro-mesoporous TiO_2-CeO_2 inverse opals. *J. Photochem. Photobiol. A Chem.* **2018**, *352*, 25–34. [CrossRef]

35. Choudhury, B.; Choudhury, A. Ce^{3+} and oxygen vacancy mediated tuning of structural and optical properties of CeO_2 nanoparticles. *Mater. Chem. Phys.* **2012**, *131*, 666–671. [CrossRef]

36. Ma, L.; Wang, D.; Li, J.; Bai, B.; Fu, L.; Li, Y. Ag/CeO_2 nanospheres: Efficient catalysts for formaldehyde oxidation. *Appl. Catal. B Environ.* **2014**, *148–149*, 36–43. [CrossRef]

37. Popovic, Z.V.; Dohcevic-Mitrovic, Z.; Konstantinovic, M.J.; Scepanovic, M. Raman scattering characterization of nanopowders and nanowires (rods). *J. Raman Spectrosc.* **2007**, *38*, 750–755. [CrossRef]

38. Natile, M.M.; Boccaletti, G.; Glisenti, A. Properties and reactivity of nanostructured CeO_2 powders: Comparison among two synthesis procedures. *Chem. Mater.* **2005**, *17*, 6272–6286. [CrossRef]

39. Davydov, A. *Molecular Spectroscopy of Oxide Catalyst Surfaces*; Sheppard, N.T., Ed.; JohnWiley & Sons Ltd.: Chichester, UK, 2003.

40. Liu, B.; Li, C.; Zhang, Y.; Liu, Y.; Hu, W.; Wang, Q.; Han, L.; Zhang, J. Investigation of catalytic mechanism of formaldehyde oxidation over three-dimensional ordered macroporous Au/CeO_2 catalyst. *Appl. Catal. B Environ.* **2012**, *111*, 467–475. [CrossRef]

41. Finos, G.; Collins, S.; Blanco, G.; Del Rio, E.; Cíes, J.M.; Bernal, S.; Bonivardi, A. Infrared spectroscopic study of carbon dioxide adsorption on the surface of cerium-gallium mixed oxides. *Catal. Today* **2012**, *180*, 9–18. [CrossRef]

42. Sing, K.S.W.; Everet, D.H.; Haul, R.A.W. Reporting Physisorption Data for gas/solid system with Special Reference to the Determination of Surface Area and Porosity. *Pure Appl. Chem.* **1985**, *57*, 603–619. [CrossRef]

43. Verma, R.; Samdarsh, S.K.; Bojja, S.; Paul, S.; Choudhury, B. A novel thermophotocatalyst of mixed-phase cerium oxide (CeO_2/Ce_2O_3) homocomposite nanostructure: Role of interface and oxygen vacancies. *Sol. Energy Mater. Sol. Cells* **2015**, *141*, 414–422. [CrossRef]

44. Jiang, D.; Wang, W.; Zhang, L.; Zheng, Y.; Wang, Z. Insights into the Surface-Defect Dependence of Photoreactivity over CeO_2 Nanocrystals with Well-Defined Crystal Facets. *ACS Catal.* **2015**, *5*, 4851–4858. [CrossRef]

45. Mena, E.; Rey, A.; Rodríguez, E.M.; Beltrán, F.J. Nanostructured CeO_2 as catalysts for different AOPs based in theapplication of ozone and simulated solar radiation. *Catal. Today* **2017**, *280*, 74–79. [CrossRef]

46. Kim, Y.I.; Atherton, S.J.; Brigham, E.S.; Mallouk, T.E. Sensitized layered metal oxide semiconductor particles for photochemical hydrogen evolution from nonsacrificial electron donors. *J. Phys. Chem.* **1993**, *97*, 11802–11810. [CrossRef]

47. Gao, X.; Jiang, Y.; Zhong, Y.; Luo, Z.; Cen, K. The activity and characterization of CeO_2-TiO_2 catalysts prepared by the sol—Gel method for selective catalytic reduction of NO with NH_3. *J. Hazard. Mater.* **2010**, *174*, 734–739. [CrossRef] [PubMed]

48. Gamboa-Rosales, N.K.; Ayastuy, J.L.; González-Marcos, M.P.; Gutiérrez-Ortiz, M.A. Oxygen-enhanced water gas shift over ceria-supported Au-Cu bimetallic catalysts prepared by wet impregnation and deposition-precipitation. *Int. J. Hydrogen Energy* **2012**, *37*, 7005–7016. [CrossRef]

49. Fiorenza, R.; Crisafulli, C.; Condorelli, G.G.; Lupo, F.; Scirè, S. $Au-Ag/CeO_2$ and $Au-Cu/CeO_2$ Catalysts for Volatile Organic Compounds Oxidation and CO Preferential Oxidation. *Catal. Lett.* **2015**, *145*, 1691–1702. [CrossRef]

50. Bêche, E.; Charvin, P.; Perarnau, D.; Abanades, S.; Flamant, G. Ce 3d XPS investigation of cerium oxides and mixed cerium oxide (Ce xTiyOz). *Surf. Interface Anal.* **2008**, *40*, 264–267. [CrossRef]

51. Ahmed, S.; Rasul, M.G.; Brown, R.; Hashib, M.A. Influence of parameters on the heterogeneous photocatalytic degradation of pesticides and phenolic contaminants in wastewater: A short review. *J. Environ. Manag.* **2011**, *92*, 311–330. [CrossRef]

52. Farré, M.J.; Franch, M.I.; Malato, S.; Ayllón, J.A.; Peral, J.; Doménech, X. Degradation of some biorecalcitrant pesticides by homogeneous and heterogeneous photocatalytic ozonation. *Chemosphere* **2005**, *58*, 1127–1133. [CrossRef]

53. Verma, A.; Toor, A.P.; Prakash, N.T.; Bansal, P.; Sangal, V.K. Stability and durability studies of TiO_2 coated immobilized system for the degradation of imidacloprid. *New J. Chem.* **2017**, *41*, 6296–6304. [CrossRef]

54. Sharma, M.V.P.; Kumari, D.V.; Subrahmanyam, M. TiO_2 supported over SBA-15: An efficient photocatalyst for the pesticide degradation using solar light. *Chemosphere* **2008**, *73*, 1562–1569. [CrossRef] [PubMed]

55. Agüera, A.; Almansa, E.; Malato, S.; Maldonado, M.I.; Fernández-Alba, A.R. Evaluation of photocatalytic degradation of Imidacloprid in industrial water by GC-MS and LC-MS. *Analusis* **1998**, *26*, 245–251. [CrossRef]

56. Redlich, D.; Shahin, N.; Ekici, P.; Friess, A.; Parlar, H. Kinetical study of the photoinduced degradation of imidacloprid in aquatic media. *Clean Soil Air Water* **2007**, *35*, 452–458. [CrossRef]

57. Kitsiou, V.; Filippidis, N.; Mantzavinos, D.; Poulios, I. Heterogeneous and homogeneous photocatalytic degradation of the insecticide imidacloprid in aqueous solutions. *Appl. Catal. B Environ.* **2009**, *86*, 27–35. [CrossRef]

58. Zang, C.; Zhang, X.; Hu, S.; Chen, F. The role of exposed facets in the Fenton-like reactivity of CeO_2 nanocrystal to the Orange II. *Appl. Catal. B Environ.* **2017**, *216*, 106–113. [CrossRef]

59. Yuan, S.; Xu, B.; Zhang, Q.; Liu, S.; Xie, J.; Zhang, M.; Ohno, T. Development of the Visible-Light Response of CeO_{2-x} with a high Ce^{3+} Content and Its Photocatalytic Properties. *ChemCatChem* **2018**, *10*, 1267–1271. [CrossRef]

60. Xiu, Z.; Xing, Z.; Li, Z.; Wu, X.; Yan, X.; Hu, M.; Cao, Y.; Yang, S.; Zhou, W. Ti^{3+}-TiO_2/Ce^{3+}-CeO_2 Nanosheet heterojunctions as efficient visible-light driven photocatalysts. *Mater. Res.* **2018**, *100*, 191–197. [CrossRef]

61. Saravanan, R.; Agarwal, S.; Gupta, V.K.; Khan, M.M.; Gracia, F.; Mosquera, E.; Narayanan, V.; Stephen, A. Line defect Ce^{3+} induced Ag/CeO_2/ZnO nanostructure for visible-light photocatalytic activity. *J. Photochem. Photobiol. A Chem.* **2018**, *353*, 499–506. [CrossRef]

62. Černigoj, U.; Štangar, U.L.; Jirkovský, J. Effect of dissolved ozone or ferric ions on photodegradation of thiacloprid in presence of different TiO_2 catalysts. *J. Hazard. Mater.* **2010**, *177*, 399–406. [CrossRef] [PubMed]

63. Zhang, A.Y.; Lin, T.; He, Y.Y.; Mou, Y.X. Heterogeneous activation of H_2O_2 by defect-engineered TiO_{2-x} single crystals for refractory pollutants degradation: A Fenton-like mechanism. *J. Hazard. Mater.* **2016**, *311*, 81–90. [CrossRef] [PubMed]

64. Du, D.; Shi, W.; Wang, L.; Zhan, J. Yolk-shell structured Fe_3O_4@void@TiO_2 as a photo-Fenton-like catalyst for the extremely efficient elimination of tetracycline. *Appl. Catal. B Environ.* **2017**, *200*, 484–492. [CrossRef]

65. Zhu, X.; Chang, Y.; Chen, Y. Toxicity and bioaccumulation of TiO_2 nanoparticle aggregates in *Daphnia magna*. *Chemosphere* **2010**, *78*, 209–215. [CrossRef] [PubMed]

66. Cantarella, M.; Gorrasi, G.; Di Mauro, A.; Scuderi, M.; Nicotra, G.; Fiorenza, R.; Scirè, S.; Scalisi, M.E.; Brundo, M.V.; Privitera, V.; et al. Mechanical milling: A sustainable route to induce structural transformations in MoS_2 for applications in the treatment of contaminated water. *Sci. Rep.* **2019**, *9*, 974. [CrossRef] [PubMed]

67. Fiorenza, R.; Bellardita, M.; D'Urso, L.; Compagnini, G.; Palmisano, L.; Scirè, S. Au/TiO_2-CeO_2 catalysts for photocatalytic water splitting and VOCs oxidation reactions. *Catalysts* **2016**, *6*, 121. [CrossRef]